nature portfolio

https://doi.org/10.1038/s41586-021-03288-7

Supplementary information

Deterministic multi-qubit entanglement in a quantum network

In the format provided by the authors and unedited

Supplementary Information for "Deterministic multi-qubit entanglement in a quantum network"

Youpeng Zhong,[1,*] Hung-Shen Chang,[1] Audrey Bienfait,[1,†] Étienne Dumur,[1,2,‡] Ming-Han Chou,[1,3] Christopher R. Conner,[1] Joel Grebel,[1] Rhys G. Povey,[1,3] Haoxiong Yan,[1] David I. Schuster,[3,1] and Andrew N. Cleland[1,2,§]

[1] *Pritzker School of Molecular Engineering, University of Chicago, Chicago IL 60637, USA*

[2] *Center for Molecular Engineering and Material Science Division, Argonne National Laboratory, Argonne IL 60439, USA*

[3] *Department of Physics, University of Chicago, Chicago IL 60637, USA*

I. DEVICE FABRICATION

The device fabrication recipe is adapted from Refs. 1–3, with some modifications to simplify the fabrication of the air-bridge crossovers.

Fabrication steps preceding definition of the qubit and coupler Josephson junctions are done on a 100 mm-diameter sapphire wafer. The wafer is then cut into four quarters, allowing for more attempts for the more delicate junction fabrication.

1. 100 nm Al base layer deposition using electron beam evaporation.

2. Base layer photolithography and dry etch with $BCl_3/Cl_2/Ar$ inductively coupled plasma (ICP). This defines the qubit capacitors, the tunable coupler wiring, and the readout and control circuitry.

3. 200 nm crossover scaffold SiO_2 deposition using photolithography, electron beam evaporation and liftoff.

4. 10 nm/150 nm Ti/Au alignment mark layer deposition using photolithography, electron beam evaporation and liftoff.

5. Josephson junction deposition using the Dolan bridge method [4] using shadow evaporation and liftoff, using a PMMA/MAA bilayer and electron beam lithography. The Al evaporated in this step does not have any galvanic contact with the base layer wiring.

6. 300 nm crossover and bandage layer: Al liftoff deposition, preceded by an *in situ* Ar ion mill. This step [5] creates the top Al layer for crossovers, as well as establishes galvanic connections between the base wiring Al from step 1 and the Josephson junctions defined in step 5.

7. Vapor HF etch to remove the SiO_2 scaffold underlying the Al crossovers from step 3.

* Present Address: Shenzhen Institute for Quantum Science and Engineering, Southern University of Science and Technology, Shenzhen 518055, China

† Present Address: Université de Lyon, ENS de Lyon, Université Claude Bernard, CNRS, Laboratoire de Physique, F-69342 Lyon, France

‡ Present Address: Université Grenoble Alpes, CEA, INAC-Pheliqs, 38000 Grenoble, France

§ Corresponding author; anc@uchicago.edu

We use 0.9 μm I-line photoresist AZ MiR 703 for all photolithography steps. The base layer lithography (step 2) uses AZ 300 MIF developer. The other steps (step 3, 4 and 6) use AZ 1:1 developer, which does not attack aluminum. Because the SiO_2 scaffold layer (step 3) and the crossover layer (step 6) here involve much thinner deposited layers than those in Refs. 1 and 3, a thick layer of AZ 703 photoresist is sufficient for the lift-off process, which greatly simplifies the fabrication recipe, as compared to the use of tri-layer positive photoresist in Ref. 3 or negative photoresist in Ref. 1. Furthermore, the crossover layer is now merged with the bandage layer [5] (step 6) here, further simplifying the fabrication process. Note the air-bridge is mechanically fragile and cannot sustain sonication.

II. CABLE-CHIP WIREBOND CONNECTIONS

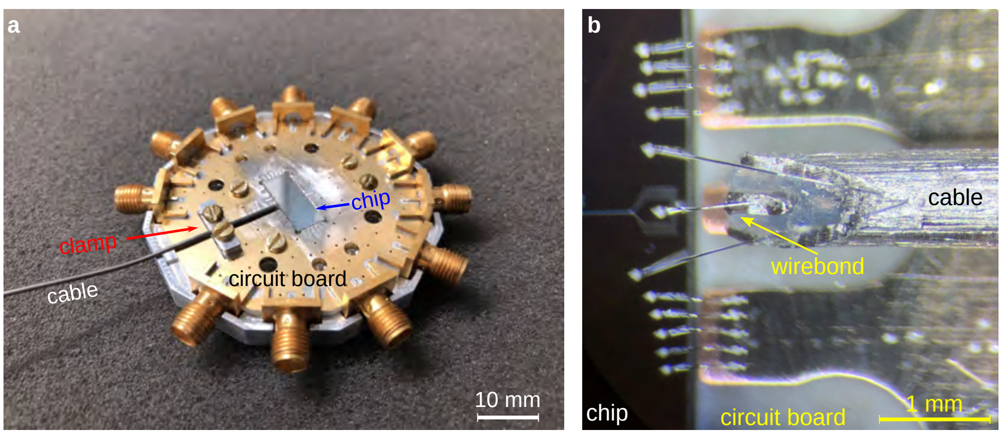

Figure S1. Cable-chip wirebond connection. **a,** Image of the sample holder consisting of a gold-plated printed circuit board, non-magnetic SMA connectors and an aluminum enclosure (the top part of which is removed here). The NbTi cable is held close to the chip, then firmly clamped to the sample holder. **b,** Image showing the wirebond connection between the coaxial cable and the processor chip.

In this experiment, we use a 1 meter long niobium-titanium (NbTi) superconducting coaxial cable (manufacturer: COAX CO., LTD., part number: SC-086/50-NbTi-NbTi) to connect the two superconducting quantum processors. To achieve a high-quality communication channel connection, we avoid the use of normal-metal connectors (e.g. SMA connectors) and instead use 25 μm diameter aluminum wirebonds to connect the cable directly to the superconducting processor chip. A sample holder specifically designed for this purpose is used here, as shown in Fig. S1a. The NbTi coaxial cable is held close to the processor chip and then firmly clamped on the sample holder with a clamp. The top part of the outer conductor and the PTFE dielectric is removed with a sharp blade to expose the inner conductor at the end of the cable, as shown in Fig. S1b. The top surfaces of the inner and outer conductors are carefully scraped with a sharp blade to create a flat surface for wirebonding. We note that niobium and its alloys are difficult to wirebond or solder to, due to the hard native oxide layer that forms naturally on the cable surface. In particular, wirebonding to the 0.2 mm diameter rounded surface of the inner conductor is especially challenging.

The quality factor of the communication channel varies in different assembled devices, depending strongly on the quality of the wirebond connection. To further explore the loss mechanism in the communication channel, we performed a separate cable test experiment, where we directly wirebond the NbTi cable to a short coplanar waveguide (CPW) line of length $\ell_c \approx 3$ mm on a test chip, see Fig. S2. A network analyzer measurement is carried out [6], yielding the quality factor Q of each standing mode (blue dots). We observe a clear trend of Q increasing with frequency in this cable test. For comparison, we also plot the Q of the standing modes measured in the experiment in the main text (orange dots), and see a similar trend, except some modes have a significantly lower Q, likely due to spurious two-level state (TLS) defects near the resonant frequency. The overall frequency dependence is consistent with a resistive dissipation channel R_s in the wirebond interface, as shown inset in Fig. S2. This could originate from a thick oxide barrier layer on the NbTi surface. For simplicity, we assume the current of a standing cable mode follows a simple cosine shape along the CPW line. In the wirebond interface, the current is $I_0 \cos(\beta_c \ell_c)$ where I_0 is the current amplitude at the shorted end, and β_c is the propagation constant for the CPW line. This current gives a power loss $P_{\text{loss}} = I_0^2 \cos^2(\beta_c \ell_c) R_s$, corresponding to a quality factor of [7]

$$Q_{\text{loss}} = \omega_m \frac{L_m I_0^2}{P_{\text{loss}}} = \omega_m \frac{L_m}{\cos^2(\beta_c \ell_c) R_s}, \tag{S1}$$

where $\omega_m/2\pi$ is the standing mode frequency and L_m the lumped element inductance of the mode (see section V). The Q of the standing mode is then given by

$$1/Q = 1/Q_{\text{loss}} + 1/Q_0, \tag{S2}$$

where Q_0 is the cable's intrinsic quality factor. Fitting this model with the cable test data, we obtain $R_s = 0.38\ \Omega$ and $Q_0 = 90.9 \times 10^3$, shown by the grey line in Fig. S2.

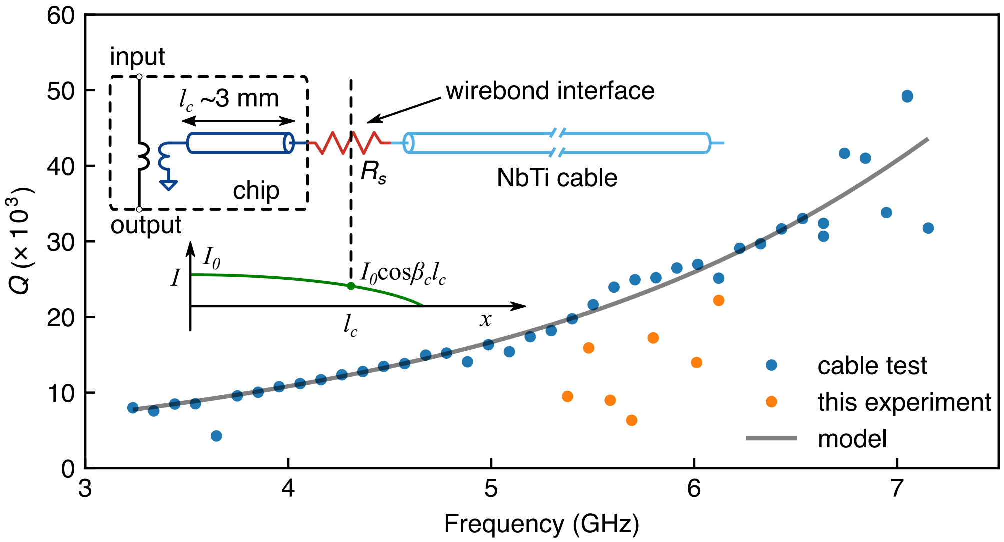

Figure S2. Channel loss from the wirebond connection. Inset: Schematic of independent measurement of coaxial cable loss, where the cable is wirebonded to a short CPW line of length $\ell_c \sim 3$ mm on a test chip. The loss in the wirebond interface is modeled as a series resistance R_s. The current distribution of a standing mode is assumed to follow a simple cosine shape along the CPW line, ignoring the transition in the wirebond interface. Blue dots represent the Q of each standing mode measured in this experiment; orange dots are from experiments in main text. Grey line is numerical model with $R_s = 0.38\ \Omega$ and $Q_0 = 90.9 \times 10^3$.

In Ref. 8, Kurpiers *et al.* reported an intrinsic Q as high as 92×10^3 for a NbTi coaxial cable made by Keycom Corp., using capacitive coupling. In Ref. 9, a NbTi cable of the same kind used in this experiment is capacitively-coupled to a 3D transmon qubit, where typical Q's of order 50×10^3 with occasional values as high as 160×10^3 were observed. The cable intrinsic Q values are quite similar, likely limited by the dielectric loss of PTFE at cryogenic temperatures.

According to the model in Fig. S2, if we adjust the coupler circuit such that $\ell_c \sim \lambda/4$, where λ is the wavelength of the chip standing mode, then $\cos(\beta_c \ell_c) \approx 0$, minimizing the loss through R_s for frequencies close to the resonant frequency of the $\lambda/4$ transformer. Alternatively, if we use a capacitive tunable coupler design [10], then the channel is open on both ends, and the loss through R_s will be small, as long as $\ell_c \ll \lambda/4$. Another approach is to minimize R_s by using an Al cable instead of NbTi, although cables clad in Al are not easily available.

III. EXPERIMENTAL SETUP

A schematic of the room-temperature electronics and the cryogenic wiring is shown in Fig. S3, similar to that in Ref. 1. We use custom digital-to-analog converter (DAC) (dual-channel, 14-bit resolution, 1 GS/s sampling rate) and analog-to-digital converter (ADC) (dual-channel, 8-bit resolution, 1 GS/s sampling rate) circuit boards for qubit control and measurement, respectively. Each control signal output and measurement signal input channel is filtered by a custom Gaussian low-pass filter with a -3 dB bandwidth of about 250 MHz.

The DAC boards can generate nanosecond-length pulses for fast qubit Z or coupler G control. The fast bias pulse is combined with a direct-current (DC) bias using a bias-tee at the 10 mK stage, where the DC bias line is filtered with an RC filter of ~ 1 MHz bandwidth at the 4 K stage and a copper powder filter at the 10 mK stage. The DAC dual-channel output can also modulate the envelope of an IQ mixer for qubit XY rotations, or to drive the readout resonator for dispersive measurements. The modulation of the IQ mixer can provide arbitrary waveform output within ± 250 MHz of its local oscillator (LO) frequency. In this experiment, 4 LOs have been used to drive IQ mixers for different purposes, where an LO at 5.6 GHz (6 GHz) carrier frequency is used to control the qubits operating at about 5.5 GHz (5.9 GHz), and an LO at 6.55 GHz (6.5 GHz) carrier frequency is used for the dispersive readout of node A (node B) respectively.

The output of the readout microwave signal is first amplified by a traveling wave parametric amplifier (TWPA) [11] at the 10 mK stage (node B does not have a TWPA for qubit readout), then amplified by a cryogenic high electron mobility transistor (Low Noise Factory) at the 4 K stage. Two cryogenic circulators with low insertion loss are added between the TWPA and the cryogenic HEMT to block reflections and thermal noise emitted from the input of the cryogenic HEMT. An additional circulator is inserted between the TWPA drive line and the processor, to avoid any unexpected excitation of the qubits from the TWPA drive signal. The cryogenic HEMT output is further amplified by two room-temperature HEMT amplifiers (Miteq Corp.), then down-converted with an IQ mixer and captured by an ADC board.

The ADC board can perform on-board multi-channel demodulation of the captured waveform, yielding a single complex value $\widetilde{I}+i\widetilde{Q}$ in the phase space for each demodulation channel

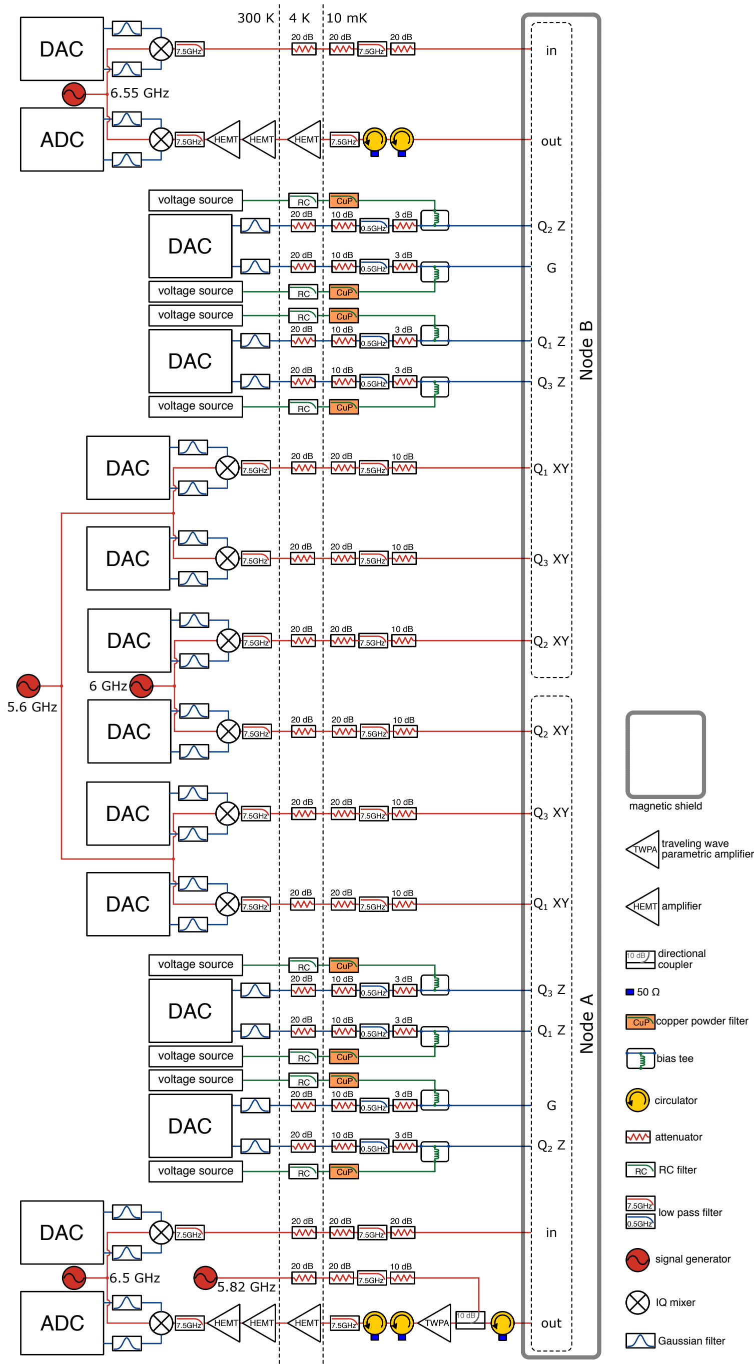

Figure S3. Schematic of the experimental setup.

from a single measurement. This allows for the simultaneous readout of multiple qubits using frequency multiplexing [12]. With calibrated discrimination criteria in the $\widetilde{I}-\widetilde{Q}$ plane, a $|g\rangle$ or $|e\rangle$ state can be assigned to each $\widetilde{I}+i\widetilde{Q}$ value. Repeating this single-shot measurement several thousand times, we obtain the qubit state probabilities.

	$f_{eg}^{\max}$ (GHz)	f_{eg}^{idle} (GHz)	η (GHz)	T_1 (μs)	T_ϕ (μs)	f_{rr} (GHz)	τ_{rr} (ns)	F_g	F_e
Q_1^A	6.04	5.5050	-0.23	12	3.4	6.5032	250	0.982	0.944
Q_2^A	6.14	5.870	-0.15	7	3.8	6.5490	350	0.981	0.935
Q_3^A	6.03	5.4882	-0.23	7	3.8	6.6045	300	0.985	0.942
Q_1^B	6.08	5.4655	-0.23	29	4.2	6.5065	300	0.995	0.955
Q_2^B	6.25	5.8950	-0.16	11	4.4	6.5560	450	0.973	0.947
Q_3^B	6.16	5.4835	-0.23	20	2.9	6.6095	300	0.984	0.953

Table S1. Qubit parameters. Here $f_{eg}^{\max}$ is the qubit maximum frequency, f_{eg}^{idle} is the qubit idle frequency, η is the qubit nonlinearity, T_1 and T_ϕ are the qubit lifetime and pure dephasing time at the idle frequency respectively, f_{rr} is the readout resonator frequency, τ_{rr} is the readout length, F_g and F_e are the readout fidelity of the $|g\rangle$ and $|e\rangle$ states respectively.

IV. DEVICE CHARACTERIZATION

A. Summary of device parameters

The parameters and typical performance of each qubit are summarized in Table S1. Note the linear inductance from the tunable coupler contributes to the total inductance of the qubit [13], reducing the maximum frequency of Q_2^n by a few hundred MHz. To counteract this effect, the size of Q_2^n's Josephson junctions was increased by 10% compared to that of the other qubits. The linear inductance from the coupler also weakens the nonlinearity of Q_2^n by about 70 MHz [13], which in turn affects the dispersive shift [14]. The readout duration for Q_2^n is correspondingly increased to compensate for this effect.

To achieve a fast dispersive readout without introducing strong Purcell decay [15], we placed a Purcell filter between the readout resonators and the readout line. The Purcell filter is essentially a shorted half-wavelength coplanar waveguide resonator, similar to that used in Refs. 16–18. The filter has a resonant frequency of about 6.5 GHz, a weak coupling to the input port (coupling $Q_c \sim 2000$) and a strong coupling to the output port (coupling $Q_c \sim 25$). With this element, we are able to perform high-fidelity qubit readout in about 300 ns, even absent a TWPA or parametric amplifier [19]. The readout fidelity for the ground state $|g\rangle$ is ~ 0.98, primarily limited by the separation error and spurious excitations [20].

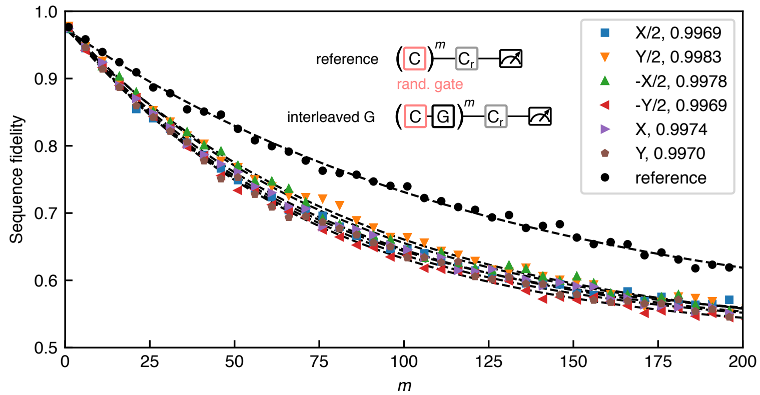

Figure S4. Single qubit randomized benchmarking for Q_1^A. Here C is a random Clifford gate and C_r is a Clifford gate that ideally restores the quantum state after the random gate sequence.

The readout fidelity of the excited state $|e\rangle$ is ~ 0.95, primarily limited by the lifetime of the qubit.

B. Single qubit gate characterization

We characterize the single qubit gate fidelities using Clifford-based randomized benchmarking (RB) [21–24]. The Clifford group is a set of rotations that evenly samples the Hilbert space, thus averaging across individual gate errors. For single-qubit RB, the Clifford group C_1 is the group of 24 rotations which preserve the octahedron in the Bloch sphere. We follow the methods in the Supplementary of Ref. 24 and implement the C_1 group with π, $\pi/2$ and $2\pi/3$ rotations. A typical RB for Q_1^A is shown in Fig. S4. Table S2 summarizes the typical single qubit gate fidelities for all qubits in this experiment.

C. iSWAP and CZ gates

The transition frequency diagram of the three qubits in each node is shown in Fig. S5a. The central qubits Q_2^n $(n = A, B)$ operate with their $g-e$ transition f_{eg} (blue) at ~ 5.9 GHz, while the other two qubits $Q_{1,3}^n$ operate at $f_{eg} \sim 5.5$ GHz (slightly detuned from one another). The $e-f$ transition f_{ef} (red) is around 5.9 GHz for Q_2^n and around 5.5 GHz for $Q_{1,3}^n$. With ~ 0.4 GHz detuning (~ 0.24 GHz detuning between the $|ee\rangle$-$|gf\rangle$ transition), the residual coupling between adjacent qubits is very small. During the quantum state transfer operation, Q_2^n is tuned to 5.798 GHz to resonantly interact with the communication mode R. At this

	X/2	-X/2	Y/2	-Y/2	X	Y	average
Q_1^A	0.9969	0.9978	0.9983	0.9969	0.9974	0.9970	0.9974
Q_2^A	0.9979	0.9969	0.9971	0.9980	0.9976	0.9973	0.9975
Q_3^A	0.9987	0.9985	0.9988	0.9970	0.9953	0.9983	0.9978
Q_1^B	0.9973	0.9990	0.9978	0.9976	0.9985	0.9981	0.9981
Q_2^B	0.9982	0.9951	0.9965	0.9959	0.9937	0.9969	0.9961
Q_3^B	0.9947	0.9968	0.9995	0.9967	0.9932	0.9983	0.9965

Table S2. Single qubit gate fidelities for all qubits in this experiment, as determined by randomized benchmarking.

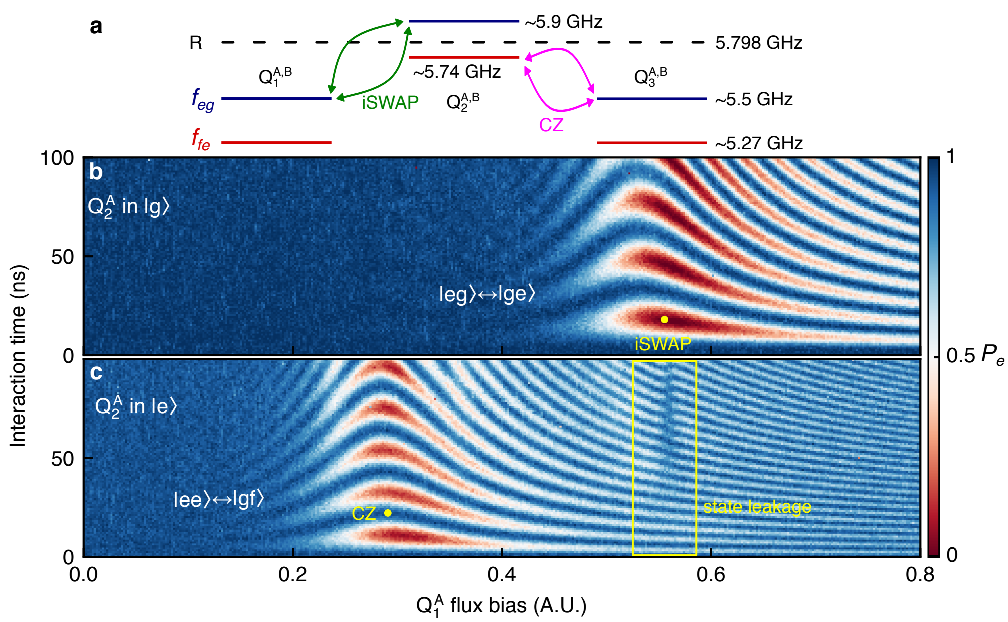

Figure S5. Implementation of two-qubit gates. **a,** Transition frequency diagram of the three qubits in each node, showing both the $g-e$ (f_{ge}) and $e-f$ (f_{ef}) transitions. The center qubits Q_2^n ($n = A, B$) are operated at ~ 5.9 GHz, and the side qubits $Q_{1,3}^n$ are operated at ~ 5.5 GHz. **b,** Vacuum Rabi oscillations for the two-qubit $|eg\rangle - |ge\rangle$ transition between Q_1^A and Q_2^A. An iSWAP gate can be implemented by enabling this oscillation for a duration of 15 ns, as marked by the yellow dot. **c,** Vacuum Rabi oscillations for the $|ee\rangle - |gf\rangle$ transition between Q_1^A and Q_2^A. A CZ gate can be implemented by enabling this oscillation for a duration of 21 ns, as marked by the yellow dot.

frequency, the detuning between Q_2^n and the side qubits $Q_{1,3}^n$ is not small enough to avoid unwanted stray coupling, so we apply detuning pulses to $Q_{1,3}^n$ to reduce their transition frequencies by about 200 MHz during this process.

To swap a quantum state from $Q_{1,3}^n$ to Q_2^n (initially in the $|g\rangle$ state), we bias $Q_{1,3}^n$ so its $g-e$ transition is resonant with that of Q_2^n, initiating vacuum Rabi oscillation between the $|eg\rangle$ and $|ge\rangle$ states, as shown in Fig. S5b. The capacitive coupling between Q_2^n and $Q_{1,3}^n$ can be accurately modeled by the Jaynes-Cummings Hamiltonian,

$$H_{j,2}^n/\hbar = g_{j,2}^n \left(\sigma_2^n \sigma_j^{n\dagger} + \sigma_2^{n\dagger}\sigma_j^n\right), \tag{S3}$$

where σ_i^n is the annihilation operator for qubit Q_i^n and $g_{j,2}/2\pi = 15.7$ MHz is the capacitive coupling strength between Q_2^n and $Q_{1,3}^n$. Initiating this interaction for the appropriate time t will evolve the initial state $|eg\rangle$ to the state $|eg\rangle \to \cos(g_{j,2}^n t)|eg\rangle - i\sin(g_{j,2}^n t)|ge\rangle$.

At $t = \tau_{\text{swap}} = \pi/2g_{j,2}^n = 15$ ns, $\cos(g_{j,2}^n t) = 0$, $\sin(g_{j,2}^n t) = 1$, we complete the $|eg\rangle \to -i|ge\rangle$ iSWAP process. Ideally, the $|ee\rangle$ state is unchanged under this gate, but as shown in Fig. S5c, due to the weak nonlinearity of Q_2^n, if both qubits are in the $|e\rangle$ state, stray coupling between the $|gf\rangle$ state and the $|ee\rangle$ state can cause state leakage during the iSWAP gate. Fortunately, in this experiment, the receiver qubit is ideally always in its $|g\rangle$ state when we transfer states using the iSWAP gate, so this state leakage is not a concern here, but will affect the quantum process tomography of the iSWAP gate. We therefore characterize the iSWAP gate with a different method, as discussed below.

To characterize the transfer efficiency of the iSWAP gate, we compare the Q_2^n $|e\rangle$ final state probability P_e from two experiments: In one experiment, we apply a π pulse to Q_2^n directly, and then measure; in the other experiment, we apply a π pulse to $Q_{1,3}^n$ and then transfer the excitation to Q_2^n using an iSWAP gate, followed by measurement. These two experiments are carried out back-to-back and repeated 1000 times. We compare the average $\langle P_e\rangle$ from the two experiments, and find that the iSWAP gate has a transfer efficiency $\eta_{\text{iSWAP}} \approx 0.99$.

A controlled-phase gate (also called a controlled-Z or CZ gate) is a conditional two-qubit gate, where typically the first qubit is the control qubit and the second qubit is the target qubit. A Z gate σ_z is applied to the target qubit, conditional on the control qubit being in

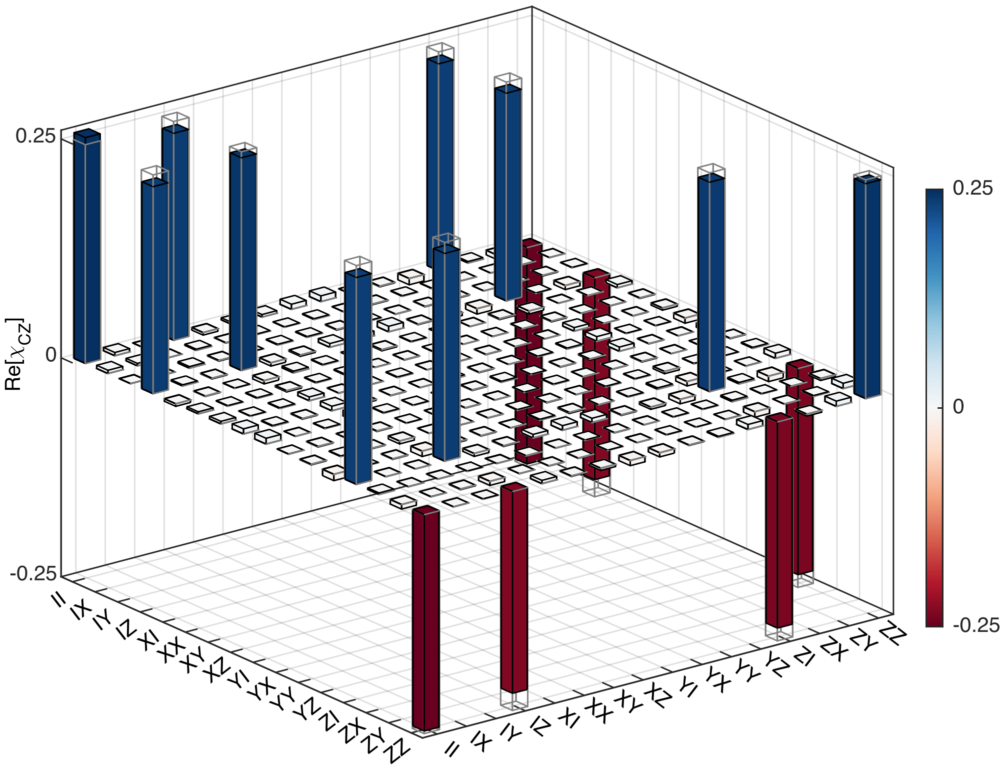

Figure S6. Quantum process tomography of the CZ gate between Q_1^A and Q_2^A. The solid color and gray outline bars are for the measured and ideal values respectively. The CZ gate has a process fidelity of 0.958 ± 0.007.

	$Q_1^A - Q_2^A$	$Q_3^A - Q_2^A$	$Q_1^B - Q_2^B$	$Q_3^B - Q_2^B$	average
$\mathcal{F}_{CZ}$	0.958(7)	0.945(8)	0.952(5)	0.944(7)	0.950(6)

Table S3. CZ gate fidelities, determined by process tomography.

the state $|e\rangle$. The unitary operator for the CZ gate can be written as

$$U_{CZ} = \begin{pmatrix} 1 & 0 & 0 & 0 \\ 0 & 1 & 0 & 0 \\ 0 & 0 & 1 & 0 \\ 0 & 0 & 0 & -1 \end{pmatrix} = |g\rangle\langle g| \otimes \mathbb{I} + |e\rangle\langle e| \otimes \sigma_z. \tag{S4}$$

From Eq. S4, we see that in fact there is no difference between the control and target qubits for this gate, thus the circuit diagram for the CZ gate takes on its symmetric form shown in Fig. S7.

Figure S7. CZ and CNOT gate diagrams.

A controlled-NOT (CNOT) gate is another fundamental two-qubit gate, where an X gate σ_x is applied to the target qubit conditional on the control qubit being in the state $|e\rangle$. The unitary operator for the CNOT gate can be written as

$$U_{CNOT} = \begin{pmatrix} 1 & 0 & 0 & 0 \\ 0 & 1 & 0 & 0 \\ 0 & 0 & 0 & 1 \\ 0 & 0 & 1 & 0 \end{pmatrix} = |g\rangle\langle g| \otimes \mathbb{I} + |e\rangle\langle e| \otimes \sigma_x. \tag{S5}$$

For superconducting qubits, the CZ gate is more straightforward to implement than the CNOT, where the latter can be realized by combining a CZ gate with two $\pi/2$ rotations, as shown in Fig. S7.

In the experiment here, the CZ gate here is implemented utilizing the $|f\rangle$ state of Q_2^n, as proposed in Ref. 25 and demonstrated in Refs. 26 and 27. When biasing $Q_{1,3}^n$ to be resonant with the $|e\rangle$-$|f\rangle$ transition frequency of Q_2^n, a vacuum Rabi oscillation between the $|ee\rangle$ and $|gf\rangle$ state can be observed, as shown in Fig. S5c. If the interaction is turned on for $\tau_{\mathrm{CZ}} = \pi/\sqrt{2}g_{j,2}^n \approx 21$ ns, $j = 1, 3$, the quantum state completes an $|ee\rangle \to -i|gf\rangle \to -|ee\rangle$ round trip and acquires a π phase relative to the other states, as required for this gate [25].

We perform quantum process tomography to characterize the CZ gate between Q_1^A and Q_2^A here, yielding the process matrix χ_{CZ} shown in Fig. S6, with a process fidelity of $\mathcal{F}_{CZ} = \mathrm{Tr}(\chi_{CZ} \cdot \chi_{CZ,\mathrm{ideal}}) = 0.958 \pm 0.007$, here $\chi_{CZ,\mathrm{ideal}}$ is the process matrix for the ideal CZ gate, and the error bar is the standard deviation of repeated measurements. The fidelities of all the CZ gates are summarized in Table S3, with an average fidelity of 0.950 ± 0.006, here the error bar is the standard deviation of the four CZ gate fidelities.

In addition to quantum process tomography, randomized benchmarking (RB) can be used to evaluate the CZ gate fidelity, as demonstrated in Refs. 24, 28–30. However, two-qubit RB involves the two-qubit Clifford group C_2, which has 11,520 elements [24], making this significantly more computationally and experimentally involved than single-qubit RB. More recently, a simpler method called cross-entropy benchmarking (XEB) has been introduced

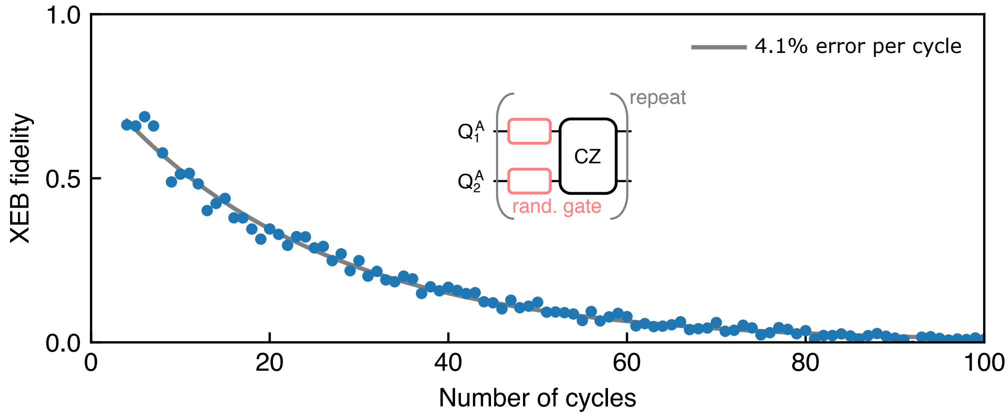

Figure S8. Cross-entropy benchmarking of the CZ gate, with an error of 4.1% per cycle.

to benchmark two-qubit gates [30], which interleaves the two-qubit gate with random single qubit gates, as shown in Fig. S8 inset. In Fig. S8 we follow the Supplementary of Ref. 30 and use the XEB technique to estimate the fidelity of the CZ gate, where we measure an error of 4.1% per cycle. Subtracting the single-qubit gate errors, the CZ gate fidelity is 0.964, in good agreement with the process tomography fidelity. Note that CZ gate fidelities > 0.99 can be achieved with an optimized adiabatic gate [24, 31] or tunable coupling [13, 30, 32].

A dynamic phase is accumulated by each qubit when performing the two-qubit gates, due to the change of the qubit frequency during the interaction. This dynamic phase can be physically corrected by applying a calibrated Z rotation. Alternatively, to simplify the control sequence, here we adjust the phase of the tomography pulses to correct for the dynamic phase shift when performing quantum state tomography. Similarly, we adjust the phase of the second $Y/2$ gate on the target qubit to correct for the dynamic phase shift when performing a CNOT gate.

D. Flux crosstalk

There are 6 qubits and 2 tunable couplers in the quantum network measured here, each of which has an independent flux control line. It is very important to mitigate the flux crosstalk between these channels, to achieve the highest fidelity qubit control and state transfer. First, we implemented a gradiometer design for the flux control line of each qubit, in order to minimize the flux crosstalk, as shown in Fig. S9a and b. We then measured the flux crosstalk between qubit pairs using Ramsey interference. We find that the crosstalk

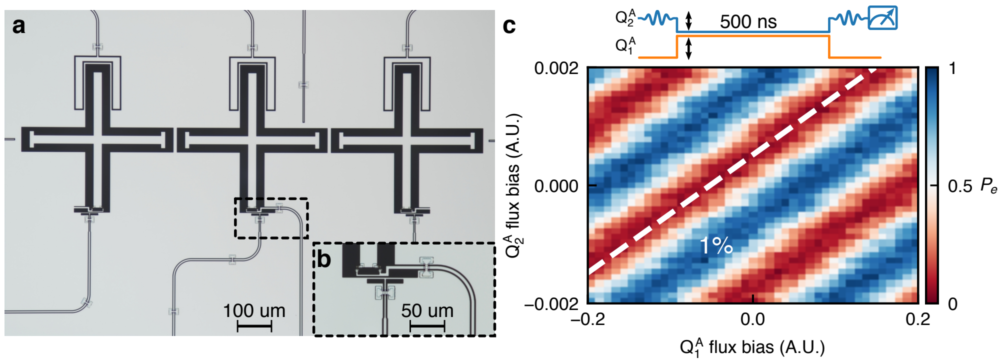

Figure S9. Measurement of qubit and coupler magnetic flux crosstalk. **a,** Xmon qubit design adopted from Ref. 33, with a gradiometer flux control line design. **b,** Magnified view of the flux control line design. **c,** Characterization of the flux crosstalk between Q_1^A and Q_2^A, using Ramsey interference. The control pulse sequence is shown on top, where the black double-headed arrows represent the effect of the control fluxes varied in the measurement. The white dashed line is a representative contour line of the data, along which the fluxes from the control lines for Q_1^A and Q_2^A cancel one another. The slope of this line, which is 1% here, represents the flux crosstalk between these two qubits.

between neighbouring qubits is about 1%, where a representative measurement in shown in Fig. S9c. The flux crosstalk between the cable-coupled qubits Q_2^n and their adjustable couplers G^n in each node is estimated to be 3-6%, using spectroscopy measurements (not shown).

V. QUBIT-CABLE COUPLING

The $\ell_{cb} = 1$ m long NbTi cable has a specific capacitance $\mathscr{C}_{cb} = 96.2$ pF/m and a specific inductance $\mathscr{L}_{cb} = 240.5$ nH/m (as provided by the cable manufacturer). The cable is galvanically connected to the tunable couplers by a short segment of CPW line of length $\ell_c \approx 2$ mm patterned on each quantum processor die. The CPW line has a specific capacitance $\mathscr{C}_{cpw} = 173$ pF/m and specific inductance $\mathscr{L}_{cpw} = 402$ nH/m. The m^{th} standing mode in the CPW-cable-CPW channel can be modeled as a lumped element series LC resonator [7], with parameters given by

$$L_m \approx \frac{1}{2}(\mathscr{L}_{cb}\ell_{cb} + 2\mathscr{L}_{cpw}\ell_c) = 121 \text{ nH}, \tag{S6}$$

$$\omega_m \approx m\omega_{\mathrm{FSR}}, \tag{S7}$$

$$C_m = \frac{1}{\omega_m^2 L_m}. \tag{S8}$$

Each qubit Q_2^n ($n = A, B$) is coupled to the channel via a tunable coupler G^n with the same design as in Ref. 1. This configuration is accurately modeled [13, 34] as a tunable inductance given by

$$M_c^n = \frac{L_g^2}{2L_g + L_w + L_T^n/\cos\delta^n}, \tag{S9}$$

where δ^n is the phase across the coupler Josephson junction, L_T^n is the coupler junction inductance at $\delta^n = 0$, $L_g = 0.2$ nH, and $L_w \approx 0.1$ nH represents the stray wiring inductance, which cannot be ignored when L_T^n becomes very small [1].

In the harmonic limit and assuming weak coupling, the coupling between qubit Q_2^n and the m^{th} mode is [13, 34]

$$g_m^n = -\frac{M_c^n}{2}\sqrt{\frac{\omega_m \omega_2^n}{(L_g + L_q^n)(L_g + L_m)}}, \tag{S10}$$

where $L_q^n \approx 8.4$ nH is the qubit Q_2^n inductance and $\omega_2^n/2\pi$ is Q_2^n's operating frequency. We see that $g_m^n \propto \sqrt{\omega_m} \propto \sqrt{m}$, a well-known result for multi-mode coupling [35]. It is experimentally more practical to approximate the coupling by a single value g^n, because as the mode number $m \sim 55 \gg 1$ near 5.8 GHz, the variation in g_m^n with m within the frequency range of interest is small.

To characterize the tunable couplers, we vary the coupler junction phase δ^n and tune the qubit Q_2^n to resonantly interact with the communication mode R, as shown in Fig. S10a. The coupling strength $g^n/2\pi$ versus δ^n is shown in Fig. S10b, which is obtained by fitting a series of vacuum Rabi oscillations similar to Fig. S10a (for details of the fitting, see Section VI). We fit the analytical model, Eq. (S10), to the data in Fig. S10b, and find that $L_T^A = 0.620$ nH and $L_T^B = 0.625$ nH. Maximum coupling occurs at the junction phase $\delta^n = \pi$, where $g_{\mathrm{max}}^A/2\pi \approx 29$ MHz and $g_{\mathrm{max}}^B/2\pi \approx 28$ MHz. The coupling can be turned off by setting $\delta^n = \pi/2$, making $L_T^n/\cos\delta^n$ very large.

It can be seen from Fig. S10a that the envelope of the vacuum Rabi oscillation decays faster as the coupling strength increases. This is attributed to the lossy wirebond interface, which not only introduces dissipation to the communication channel, but also affects the qubit coherence. Here we use a phenomenological model, shown at the top of Fig. S10c, to characterize the qubit loss at different coupling strengths, where we simply assume a

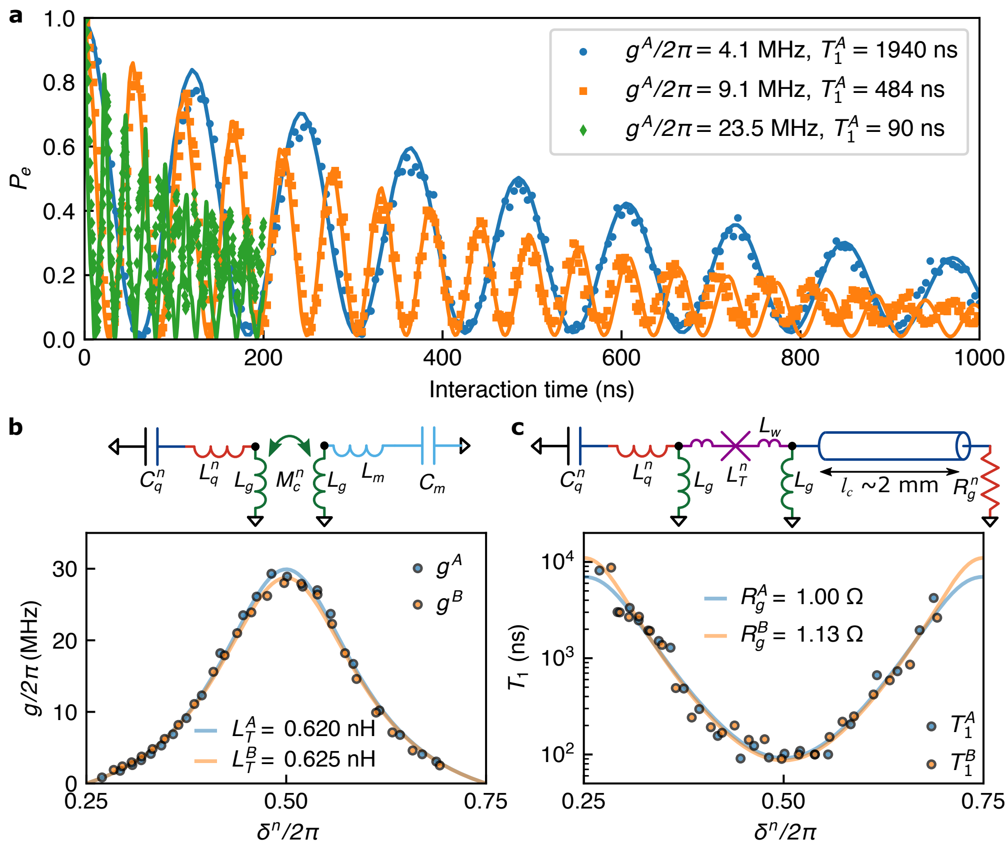

Figure S10. Tunable coupler characterization. **a,** Vacuum Rabi oscillations between qubit Q_2^A and the communication mode R at different coupling strength $g^A/2\pi$. Fitting the data gives $g^A/2\pi$ and the qubit lifetime T_1^A during the interaction. **b,** $g^n/2\pi$ versus δ^n. Top: lumped-element linear circuit model for the inductive coupling between the qubit Q_2^n and the communication mode R, which is modeled as a series LC resonator. **c,** Q_2^n lifetime T_1^n versus δ^n during the interaction. Top: phenomenological circuit model for calculating the qubit loss, assuming a loss channel R_g^n shunting the wirebond connection to ground.

lumped resistor R_g^n shunting the wirebond interface to ground. We fit the model with the measured qubit T_1^n (log scale), and find that the model agrees very well with the data, with $R_g^A = 1.00\ \Omega$ and $R_g^B = 1.13\ \Omega$.

VI. NUMERICAL SIMULATIONS

The full quantum system can be modeled with the following rotating-frame, multi-qubit, multi-mode communication channel Hamiltonian:

$$\begin{aligned} H/\hbar = & \sum_{i=1,2,3}^{n=A,B} \Delta\omega_i^n \sigma_i^{n\dagger} \sigma_i^n + \sum_{m=1}^{M} \left(m - \frac{M+1}{2} \right) \omega_{\mathrm{FSR}} a_m^\dagger a_m \\ & + \sum_{n=A,B} \sum_{j=1,3} g_{j,2}^n \left(\sigma_2^n \sigma_j^{n\dagger} + \sigma_2^{n\dagger} \sigma_j^n \right) \\ & + \sum_{m=1}^{M} g^A \left(\sigma_2^A a_m^\dagger + \sigma_2^{A\dagger} a_m \right) + \sum_{m=1}^{M} (-1)^m g^B \left(\sigma_2^B a_m^\dagger + \sigma_2^{B\dagger} a_m \right), \end{aligned} \tag{S11}$$

where σ_i^n and a_m are the annihilation operators for qubit Q_i^n and the m^{th} standing-wave mode respectively, $\Delta\omega_i^n$ is the qubit frequency detuning with respect to the rotating frame frequency, and M is the number of standing modes included in the simulation (always chosen to be an odd number). The rotating frame frequency is set at the center of the standing-mode frequencies, i.e. for mode number $m = (M+1)/2$. Note the sign of g^B alternates with the mode number m due to the parity dependence of the standing wave mode [36, 37]. In this experiment, not all components are involved simultaneously, and in certain cases the full Hamiltonian can be simplified.

In Fig. 2b in the main text, where only Q_2^A and the standing modes are interacting, the Hamiltonian can be simplified to

$$H/\hbar = \sum_{m=1}^{M} \left(m - \frac{M+1}{2} \right) \omega_{\mathrm{FSR}} a_m^\dagger a_m + \sum_{m=1}^{M} g^A \left(\sigma_2^A a_m^\dagger + \sigma_2^{A\dagger} a_m \right), \tag{S12}$$

where we choose $M = 5$ standing modes, with the third mode $m = 3$ the communication mode R, and Q_2^A is assumed to be on resonant with R such that $\Delta\omega_2^A = 0$. Decoherence is taken into account using the Lindblad master equation. The quantum state evolution is calculated using QuTiP [38]. The five standing modes included in the model here have measured lifetimes of 256 ns, 177 ns, 473 ns, 200 ns, and 370 ns respectively. We first compare the numerical simulations using the qubit intrinsic lifetime $T_1 = 7$ us, and find discrepancies with the data (see the grey line in Fig. 2b of the main text). As discussed in Section II, the loss in the channel is dominated by the wirebond interface. Changing the coupler inductance does not change the participation of the lossy wirebond interface in the channel, so the lifetime of the standing modes should not be affected by the coupling strength. On the other hand, when the coupling is turned on, the qubit is exposed to the lossy wirebond interface, introducing a new loss channel to the qubit coherence. This unwanted side-effect is characterized by the phenomenological circuit model shown in Section V. We fit the master equation simulation to the experimental data and find that the qubit T_1 is decreased to 1.4 μs during the interaction (red line in Fig. 2b in the main text). Similarly, we fit a series of vacuum Rabi oscillations, as shown in Fig. S10a, to obtain the coupling strength $g^n/2\pi$ (Fig. S10b) and the qubit lifetime T_1^n (Fig. S10c) at different coupler junction phases δ^n.

In Fig. 2c in the main text, where the side qubits $Q_{1,3}^n$ are tuned far in frequency from Q_2^n, the state transfer process can be modeled with the simplified Hamiltonian:

$$\begin{aligned} H/\hbar = &\sum_{n=A,B} \Delta\omega_2^n \sigma_2^{n\dagger}\sigma_2^n + \sum_{m=1}^{M}\left(m - \frac{M+1}{2}\right)\omega_{\mathrm{FSR}} a_m^\dagger a_m \\ &+ \sum_{m=1}^{M} g^A\left(\sigma_2^A a_m^\dagger + \sigma_2^{A\dagger} a_m\right) + \sum_{m=1}^{M}(-1)^m g^B\left(\sigma_2^B a_m^\dagger + \sigma_2^{B\dagger} a_m\right), \end{aligned} \tag{S13}$$

where we include $M = 5$ standing modes in the simulations, and R is the third mode, $m = 3$. Ideally, for the hybrid state transfer scheme [39], both qubits Q_2^n should be resonant with R, such that $\Delta\omega_2^n = 0$, and the coupling g^A and g^B should be set to the same coupling strength g_0 simultaneously for a duration τ. In the experiment, we vary the qubit frequencies as well as the relative amplitude and delay between g_A and g_B, to optimize the transfer fidelity. It is found that a higher fidelity is achieved with a delay of $\Delta\tau = 13$ ns between the initial turn-on for g_A and g_B (in other words, both g_A and g_B are turned on for a duration of τ, but g^B is turned on 13 ns later than g^A). With this experimentally-optimized $\Delta\tau$, we fit the model to the data shown in Fig. 2c in the main text, and find that $\Delta\omega_2^A/2\pi = -0.95$ MHz, $\Delta\omega_2^B/2\pi = -1.79$ MHz, $g_A/2\pi = 4.08$ MHz and $g_B/2\pi = 4.06$ MHz (these are the parameters for the grey line in Fig. 2c in the main text).

In Fig. 3b of the main text, the numerical ρ^A is calculated using the CZ gate process matrix χ_{CZ} measured in Section IV C, assuming the single-qubit rotation gates are ideal (using their measured fidelities has almost no impact on the results). The numerical GHZ state fidelity is 0.938, agreeing well with the experiment. The prepared GHZ state fidelity is primarily limited by the CZ gate fidelity, which could be improved by using an optimized adiabatic gate [24, 31] or using tunable coupling [13, 30, 32]. Some one-step GHZ state preparation methods utilizing a common bus resonator may also be able to prepare high-

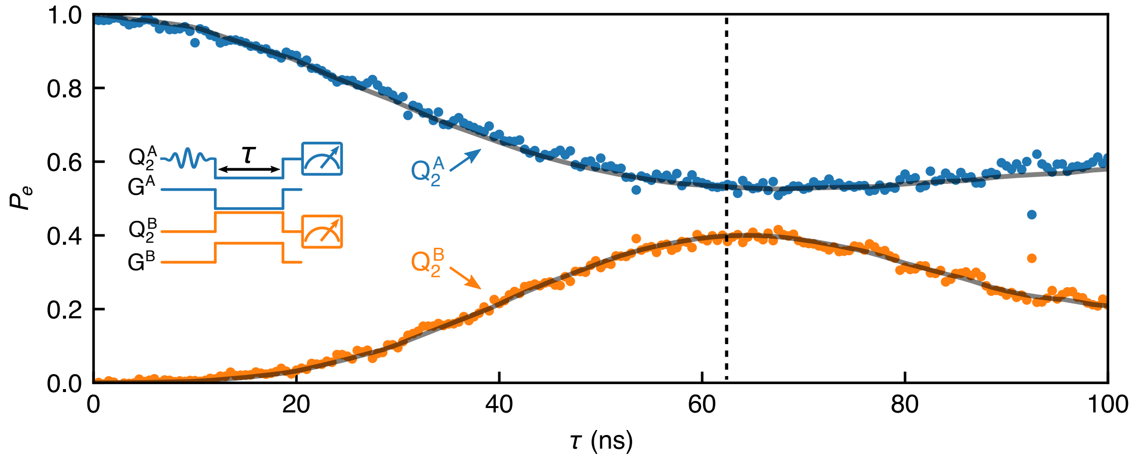

Figure S11. The “ST/2” process, where half a photon is sent from node A to node B. The control pulse sequence here is similar to that in Fig. 2c in the main text, except the coupling strength g^A and g^B, the interaction time τ and the delay $\Delta\tau$, are experimentally tuned to optimize the Bell state fidelity. The dashed line marks the point where the Bell state fidelity is optimal.

fidelity GHZ states [40, 41]. In Fig. 3c of the main text, the numerical ρ^B is calculated by applying the state transfer process $\chi^{\otimes 3}$ and the decoherence process to ρ^A from Fig. 3b. The fidelity of ρ^B is primarily limited by the state transfer fidelity $\mathcal{F}^p$, which might be improved by optimizing the coupler circuit design or using a coaxial cable made with different superconducting material, e.g. aluminium, as discussed in Section II.

In Fig. 4b in the main text, the control pulse for “ST/2” is similar to that for “ST” as shown in Fig. 2c inset, except the coupling strength g^A and g^B, the interaction time τ and the delay $\Delta\tau$, are experimentally tuned to optimize the Bell state fidelity. With $\Delta\tau = 5$ ns, as determined experimentally, we fit the data in Fig. S11, which is similar to Fig.2c in the main text, and obtain $\Delta\omega_2^A/2\pi = 4.7$ MHz, $\Delta\omega_2^B/2\pi = 5.4$ MHz, $g_A/2\pi = 2.89$ MHz and $g_B/2\pi = 6.11$ MHz. The numerical Bell state fidelity is 0.915, agreeing well with the experiment. This Bell state fidelity is primarily limited by the channel loss.

In Fig. 4c, we calculate the theoretical ρ_{II} by applying χ_{CZ} (measured in Section IV C) to ρ_I from Fig. 4b, assuming the single qubit rotation gates are ideal.

In Fig. 4d, we calculate the theoretical ρ_{III} by applying χ_{CZ} and decoherence process to ρ_{II} from Fig. 4c, again assuming the single-qubit rotation gates are ideal. The decoherence process is applied to Q_1^n to account for the idling of 70 ns during the application of CNOT gates to Q_3^n. The fidelity of ρ_{II} and ρ_{III} is primarily limited by the fidelity of ρ_I and the CZ gates.

[1] Zhong, Y. P. *et al.* Violating Bell's inequality with remotely connected superconducting qubits. *Nature Physics* **15**, 741–744 (2019).

[2] Kelly, J. S. *Fault-tolerant superconducting qubits*. Ph.D. thesis, University of California Santa Barbara (2015).

[3] Dunsworth, A. *et al.* A method for building low loss multi-layer wiring for superconducting microwave devices. *Applied Physics Letters* **112**, 063502 (2018).

[4] Dolan, G. J. Offset masks for lift-off photoprocessing. *Applied Physics Letters* **31**, 337–339 (1977).

[5] Dunsworth, A. *et al.* Characterization and reduction of capacitive loss induced by sub-micron Josephson junction fabrication in superconducting qubits. *Applied Physics Letters* **111**, 022601 (2017).

[6] Megrant, A. *et al.* Planar superconducting resonators with internal quality factors above one million. *Applied Physics Letters* **100**, 113510 (2012).

[7] Pozar, D. M. *Microwave engineering* (Wiley, 2011), fourth edn.

[8] Kurpiers, P., Walter, T., Magnard, P., Salathe, Y. & Wallraff, A. Characterizing the attenuation of coaxial and rectangular microwave-frequency waveguides at cryogenic temperatures. *EPJ Quantum Technology* **4**, 1–15 (2017).

[9] Burkhart, L. D. *et al.* Error-detected state transfer and entanglement in a superconducting quantum network. *arXiv preprint arXiv:2004.06168* (2020).

[10] Yan, F. *et al.* Tunable coupling scheme for implementing high-fidelity two-qubit gates. *Physical Review Applied* **10**, 054062 (2018).

[11] Macklin, C. *et al.* A near-quantum-limited Josephson traveling-wave parametric amplifier. *Science* **350**, 307–310 (2015).

[12] Chen, Y. *et al.* Multiplexed dispersive readout of superconducting phase qubits. *Applied Physics Letters* **101**, 182601 (2012).

[13] Chen, Y. *et al.* Qubit architecture with high coherence and fast tunable coupling. *Physical Review Letters* **113**, 220502 (2014).

[14] Koch, J. *et al.* Charge-insensitive qubit design derived from the Cooper pair box. *Physical Review A* **76**, 042319 (2007).

[15] Houck, A. *et al.* Controlling the spontaneous emission of a superconducting transmon qubit. *Physical Review Letters* **101**, 080502 (2008).

[16] Satzinger, K. J. *et al.* Quantum control of surface acoustic-wave phonons. *Nature* **563**, 661–665 (2018).

[17] Bienfait, A. *et al.* Phonon-mediated quantum state transfer and remote qubit entanglement. *Science* **364**, 368–371 (2019).

[18] Jeffrey, E. *et al.* Fast accurate state measurement with superconducting qubits. *Physical Review Letters* **112**, 190504 (2014).

[19] Vijay, R., Slichter, D. & Siddiqi, I. Observation of quantum jumps in a superconducting artificial atom. *Physical Review Letters* **106**, 110502 (2011).

[20] Walter, T. *et al.* Rapid high-fidelity single-shot dispersive readout of superconducting qubits. *Physical Review Applied* **7**, 054020 (2017).

[21] Ryan, C., Laforest, M. & Laflamme, R. Randomized benchmarking of single-and multi-qubit control in liquid-state NMR quantum information processing. *New Journal of Physics* **11**, 013034 (2009).

[22] Brown, K. R. *et al.* Single-qubit-gate error below $\mathbf{10^{-4}}$ in a trapped ion. *Physical Review A* **84**, 030303 (2011).

[23] Magesan, E. *et al.* Efficient measurement of quantum gate error by interleaved randomized benchmarking. *Physical Review Letters* **109**, 080505 (2012).

[24] Barends, R. *et al.* Superconducting quantum circuits at the surface code threshold for fault tolerance. *Nature* **508**, 500–503 (2014).

[25] Strauch, F. W. *et al.* Quantum logic gates for coupled superconducting phase qubits. *Physical Review Letters* **91**, 167005 (2003).

[26] DiCarlo, L. *et al.* Preparation and measurement of three-qubit entanglement in a superconducting circuit. *Nature* **467**, 574–578 (2010).

[27] Yamamoto, T. *et al.* Quantum process tomography of two-qubit controlled-Z and controlled-NOT gates using superconducting phase qubits. *Physical Review B* **82**, 184515 (2010).

[28] Gaebler, J. P. *et al.* Randomized benchmarking of multiqubit gates. *Physical Review Letters* **108**, 260503 (2012).

[29] Córcoles, A. D. *et al.* Process verification of two-qubit quantum gates by randomized benchmarking. *Physical Review A* **87**, 030301 (2013).

[30] Arute, F. *et al.* Quantum supremacy using a programmable superconducting processor. *Nature* **574**, 505–510 (2019).

[31] Martinis, J. M. & Geller, M. R. Fast adiabatic qubit gates using only σ_z control. *Physical Review A* **90**, 022307 (2014).

[32] Xu, Y. *et al.* High-fidelity, high-scalability two-qubit gate scheme for superconducting qubits. *Physical Review Letters* **125**, 240503 (2020).

[33] Barends, R. *et al.* Coherent Josephson qubit suitable for scalable quantum integrated circuits. *Physical Review Letters* **111**, 080502 (2013).

[34] Geller, M. R. *et al.* Tunable coupler for superconducting Xmon qubits: Perturbative nonlinear model. *Physical Review A* **92**, 012320 (2015).

[35] Sundaresan, N. M. *et al.* Beyond strong coupling in a multimode cavity. *Physical Review X* **5**, 021035 (2015).

[36] Pellizzari, T. Quantum networking with optical fibres. *Physical Review Letters* **79**, 5242 (1997).

[37] Vogell, B., Vermersch, B., Northup, T., Lanyon, B. & Muschik, C. Deterministic quantum state transfer between remote qubits in cavities. *Quantum Science and Technology* **2**, 045003 (2017).

[38] Johansson, J., Nation, P. & Nori, F. QuTiP: An open-source Python framework for the dynamics of open quantum systems. *Computer Physics Communications* **183**, 1760–1772 (2012).

[39] Wang, Y.-D. & Clerk, A. A. Using dark modes for high-fidelity optomechanical quantum state transfer. *New Journal of Physics* **14**, 105010 (2012).

[40] Zheng, S.-B. One-step synthesis of multiatom Greenberger-Horne-Zeilinger states. *Physical Review Letters* **87**, 230404 (2001).

[41] Song, C. *et al.* 10-qubit entanglement and parallel logic operations with a superconducting circuit. *Physical Review Letters* **119**, 180511 (2017).